International Journal of Fatigue 163 (2022) 107022

Contents lists available at ScienceDirect

International Journal of Fatigue

journal homepage: www.elsevier.com/locate/ijfatigue

Surface roughness effect on multiaxial fatigue behavior of additively manufactured Ti6Al4V alloy

Danilo A. Renzo [a,*], Carmine Maletta [a], Emanuele Sgambitterra [a], Franco Furgiuele [a], Filippo Berto [b]

[a] DIMEG – Dept. of Mechanical, Energy and Management Engineering, University of Calabria, 87036 Rende, Italy
[b] NTNU – Norwegian University of Science and Technology, 7491 Trondheim, Norway

ARTICLE INFO

Keywords:
Multiaxial fatigue
Additive manufacturing
Titanium alloy
Digital image correlation

ABSTRACT

Additive manufacturing (AM) is a special technology that offers several advantages compared to the conventional methodologies. For instance, it allows to build components with complex geometry, difficult to make in a different way, build integrated parts deleting joining issues, etc. However, its application in engineering fields is still limited because the dependency between the mechanical properties of the obtained components and the manufacturing parameters is not in depth understood. Improve the performances of AM components, under static and dynamic loadings, is crucial to ensure their durability and reliability and in recent years it became a challenging research field. In this work, the effect of the surface roughness on the multiaxial fatigue resistance of Ti6Al4V thin-walled tubular samples, made by the Selective Laser Melting (SLM) process, was investigated. In particular, experiments under combined axial–torsional loadings were carried out on two batches of samples, made by different surface roughness (machined and as built samples). Maximum valley depth R_v was used as a representative parameter of the surface roughness as it geometrically represents a stress concentration zone where crack initiates and propagates. An effective strain intensity factor range, based on the modified Smith Watson and Topper (MSWT) model, that includes the roughness parameter R_v, is proposed and used for a better correlation of the fatigue data. To prove the reliability of the proposed model, the Socie and the Reddy & Fatemi effective strain-based intensity factor range were also used but a bigger scattering of results was observed. The MSWT model was also applied to predict the failure plane and the obtained results were compared with the predictions of the Fatemi-Socie model. Results revealed that, for SLM Ti6Al4V alloy components, the MSWT model is more accurate.

1. Introduction

Ti6Al4V alloy is known as the most popular titanium alloy for its high strength, low density, high fracture toughness, high corrosion resistance, and biocompatible features [1]. Conventional methods as forging, casting, extrusion and rolling of bulk material followed by subsequent machining allow to obtain components with different shapes [1]. The main disadvantages of these processes are the high manufacturing cost, production time and wasting material. In the last years, technology improvements were done in the processing of Ti6Al4V components thanks to the additive manufacturing technique. This latter offers several benefits compared to the traditional manufacturing processes [2]. The first advantage is the high design freedom. In fact, it allows to produce components with complex geometries with near-net-shape and also designs lattice structures with different densities [3]. An additional advantage is the possibility to produce integrated parts, eliminating welding/joints, realizing structures less prone to leaking [4]. Thanks to these features, AM technology is widely used in several engineering fields as aerospace [7], automotive and biomedical where the realization of customized components, in terms of geometry and dimension [5,6], for repairing hip, bonds, skull and spine is always a crucial requirement. The main additive manufacturing methods are the powder bed fusion (PBF) and directed energy deposition (DED). In the first case, two different energy sources can be used: i) laser beam, known as Selective Laser Melting, and ii) electron beam, known as Electron Beam Melting (EBM) [8,9]. Process parameters have a strong influence on the performance of AM materials, especially when dealing with fatigue resistance. In fact, they highly affect the final microstructure, the surface roughness, the porosity, the anisotropy and the residual stresses

* Corresponding author.
E-mail address: danilo.renzo@unical.it (D.A. Renzo).

https://doi.org/10.1016/j.ijfatigue.2022.107022
Received 20 January 2022; Received in revised form 22 April 2022; Accepted 18 May 2022
Available online 24 May 2022

Nomenclature

AM	Additive manufacturing/manufactured
a	Material-dependent constant of the MSWT model
a_0	Initial half crack length
$\overline{b}$	Effective fatigue strength exponent
$\overline{b}_0$	Effective fatigue shear strength exponent
$\overline{c}$	Effective fatigue ductility exponent
$\overline{c}_0$	Effective fatigue shear ductility exponent
D_{FS}	Fatemi-Socie damage parameter
D_{MSWT}	MSWT damage parameter
DIC	Digital image correlation
E	Young's modulus
F_I	Geometry factor for mode I
F_{II}	Geometry factor for mode II
G	Shear modulus
k	Fatemi-Socie material constant
LOF	Lack-of-fusion
$MSWT$	Modified Smith Watson and Topper
N_f	Number of cycles to failure
R	Load ratio
R_a	Average roughness
R_t	Maximum peak of surface roughness
R_v	Maximum valley surface roughness
$\overline{S}_f$	Effective fatigue strength
SIF	Stress/strain intensity factor
S_y	Tensile yield strength
S_{sf}	Shear fatigue strength
S_{sy}	Shear yield strength
S_u	Ultimate tensile strength
S_{su}	Ultimate shear strength
$\gamma_{z\vartheta}$	Circumferential shear strain
$\Delta K_{eq}(\varepsilon)$	Effective strain-based intensity factor range
ΔK_{CPA}	Reddy & Fatemi effective strain-based intensity factor range
ΔK_{MSWT}	MWST effective strain-based intensity factor range
$\Delta\varepsilon$	Normal strain range
$\Delta\gamma$	Shear strain range
$\Delta\gamma_{max}$	Maximum shear strain range
$\Delta\varepsilon_e$	Elastic normal strain range
$\Delta\gamma_e$	Elastic shear strain range
ε_z	Normal strain
ε_ϑ	Circumferential strain
$\overline{\varepsilon}_a$	Effective elastic strain amplitude
ν_e	Elastic Poisson' ratio
ν_p	Plastic Poisson' ratio
$\overline{\nu}$	Effective Poisson' ratio
σ_a	Axial stress amplitude
σ_m	Axial mean stress
$\sigma_{n,max}$	Maximum normal stress
$\overline{\sigma}_a$	Equivalent stress amplitude
$\overline{\sigma}_m$	Equivalent mean stress
$\overline{\sigma}_{max}$	Maximum equivalent stress
$\overline{\sigma}_f^{'}$	Effective fatigue strength coefficient
τ_a	Shear stress amplitude
τ_m	Shear mean stress
$\overline{\tau}_f^{'}$	Effective fatigue shear strength coefficient
θ	Material plane orientation
θ_P	Maximum normal stress plane orientation
θ_{CP}	Critical plane orientation

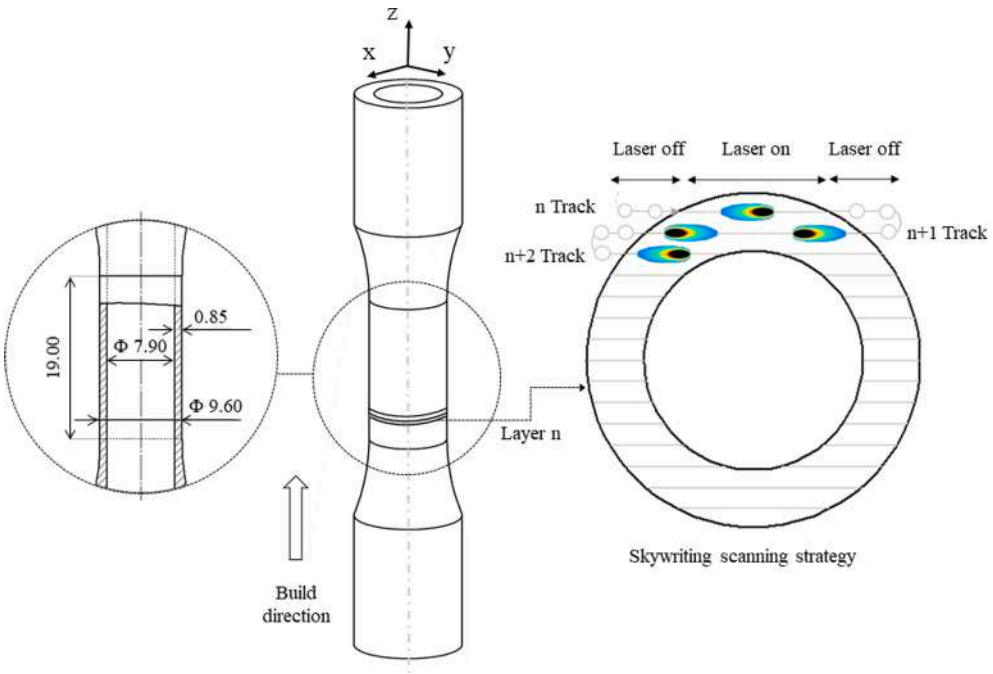

Fig. 1. Thin-walled tubular sample geometry with nominal dimensions in millimeters and schematic representation of skywriting scanning strategy.

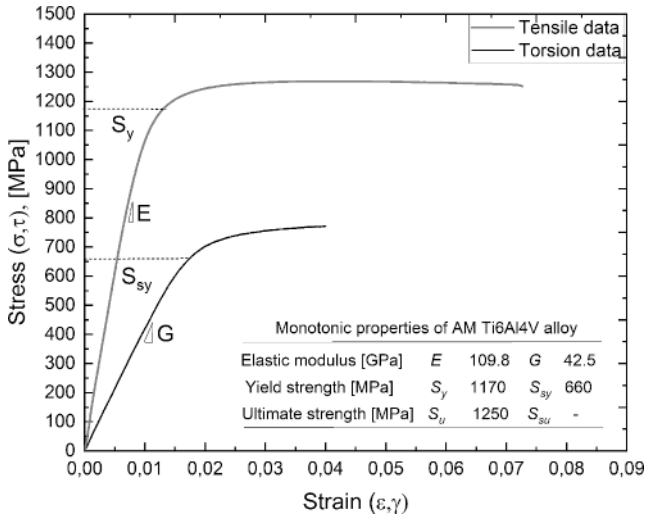

Fig. 2. Monotonic stress–strain and shear stress-shear strain curves of AM machined sample.

[10]. In order to get a better control on the final product, different scanning strategies were developed. For instance, Mancisidor et al. [12] observed a reduction of residual porosity, typically due to a higher interaction time between the laser and the powder [11], using the skywriting strategy. To control the surface roughness of AM component, instead, parameters as the power beam, material thickness, scanning rate and hatch distance have to be considered. The surface quality is also affected by the type of additive process, e.g., PBF or DED [13], as well as the geometry and build orientation [14–16]. Typically, surface roughness is categorized as primary roughness, resulting from solidification of the melt pool, and secondary roughness, resulting from partly melted powder [17]. Post-treatments such as milling, grinding, vibration assisted grinding, micro-machining, abrasive flow machining, blasting, and chemical treatment can be used to improve surface roughness up to values close to 0.9 μm, compared to the as built samples (15–30 μm) [13,18,19]. Several studies demonstrated [16–21] that surface roughness represents a detrimental factor for the fatigue performance. Sanaei et al. [16] showed that the fatigue strength increase with a decrease in surface roughness and the effect of this latter is more considerable for components with small internal defects and gross lamellar microstructure. Zhang et al. [19] evaluated the effect of surface roughness effects on multiaxial fatigue behavior developing also a fracture mechanism model that incorporates the maximum valley depth of surface roughness profile for the correlation of experimental fatigue data of AM Ti6Al4V alloy. Pegues et al. [20] showed that in the samples with a smaller diameter the effect of surface roughness on the high cycle fatigue strength is greater. Greitermeier et al. [21] observed that the higher surface roughness of AM Ti6Al4V sample is a dominant parameter for the low fatigue performance, and they concluded that the cracks initiation starts from the surface roughness valleys where acts the stress concentration points and not from the internal cracks or non-homogeneous microstructure.

In this paper, the effect of surface roughness on the multiaxial fatigue life of SLM samples was analyzed. Proportional and nonproportional multiaxial fatigue tests were carried out using machined and as built thin-walled tubular samples. A comparative analysis of the cyclic fatigue properties is reported. Considering the synergistic effect of roughness with the multiaxial state of stress, an effective strain intensity factor range based on the modified Smith Watson and Topper criterion that incorporates the roughness parameter R_v is proposed and used to improve the correlation of fatigue data. The surface of the samples was also investigated by scanning electron microscopy (SEM) to analyze the crack orientation under in-phase and 90° out-of-phase loading. Results show that the crack growth occurs along the slip systems aligned with the maximum normal stress plane. A minor prediction capacity of the failure plane orientation and the fatigue life was obtained using the

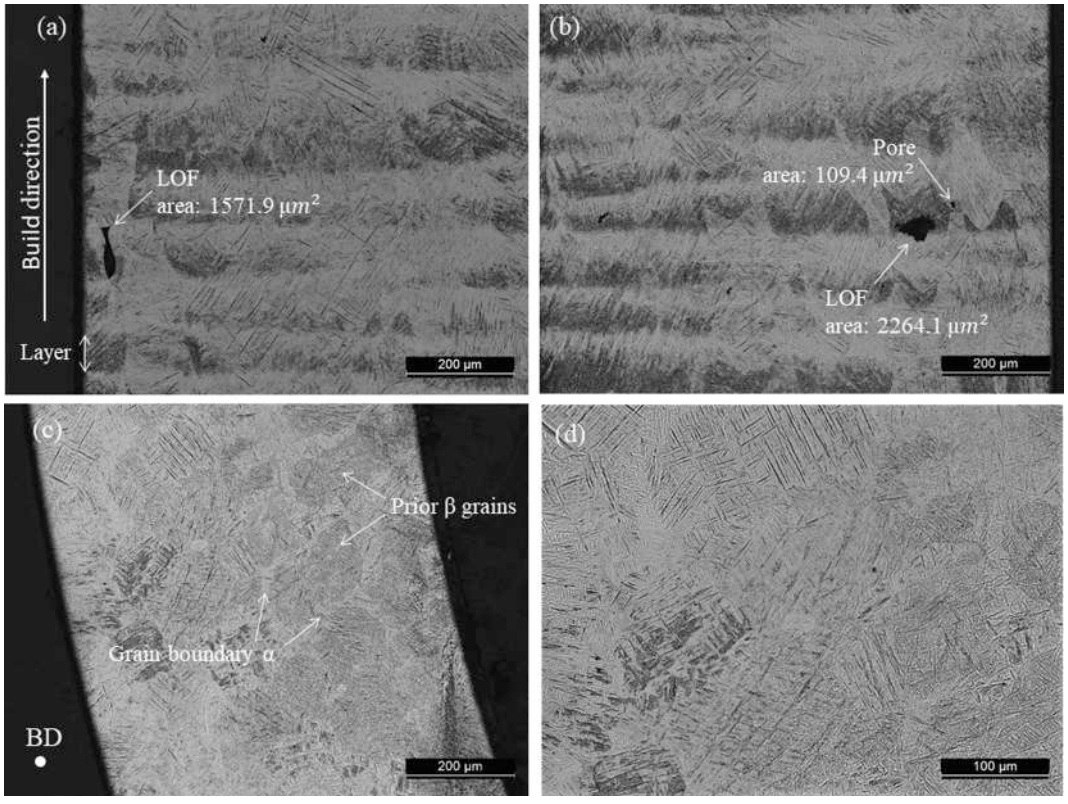

Fig. 3. Morphology microstructure of SLM Ti6Al4V alloy: (a) and (b) pores and LOF defects; (c) prior-β grains structures; (d) α + β lamellae structure.

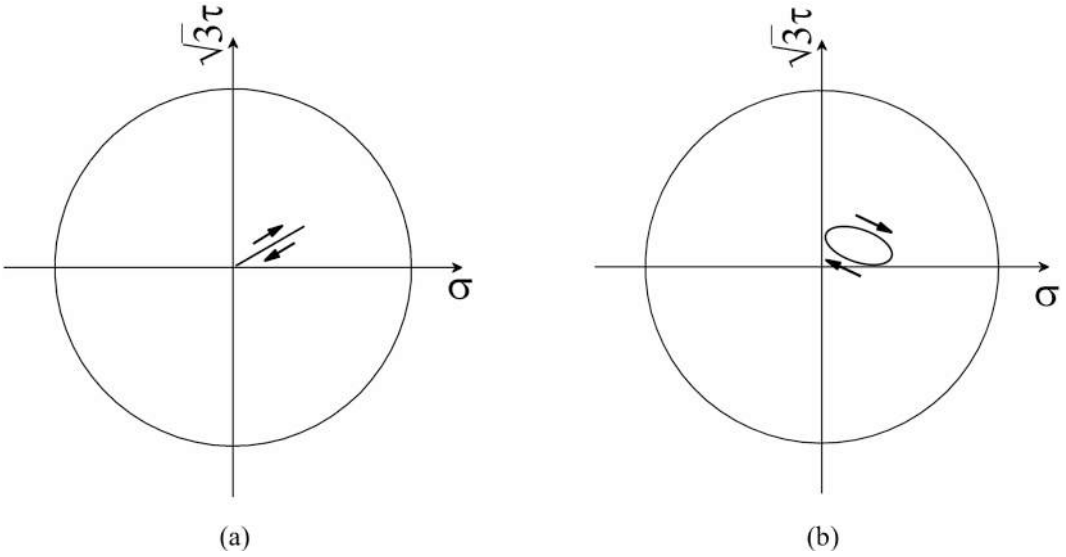

Fig. 4. Imposed stress paths in the von Mises yield surface in σ – $\sqrt{3}\tau$ stress space: (a) in-phase axial and torsional loading; (b) 90° out-of-phase axial and torsional loading.

Table 1
Multiaxial fatigue test conditions.

Load type	$\frac{\tau}{\sigma}$	Axial stresses [MPa]		Torsional stresses [MPa]		Equivalent von Mises stresses [MPa]			$\frac{\overline{\sigma}_{max}}{S_u}$ (%)
		σ_a	σ_m	τ_a	τ_m	$\overline{\sigma}_a$	$\overline{\sigma}_m$	$\overline{\sigma}_{max}$	
Additive manufactured, Machined									
IP	$\sqrt{3}/3$	220.4	243.6	127.3	140.7	311.7	344.5	656.3	52.5
IP	$\sqrt{3}/3$	209.9	232	121.2	134	296.9	328.1	625.0	50
IP	$\sqrt{3}/3$	199.4	220.4	115.1	127.3	282	311.7	593.8	47.5
IP	$\sqrt{3}/3$	188.9	208.8	109.1	120.6	267.2	295.3	562.5	45
IP	$\sqrt{3}/3$	178.4	197.2	103	113.9	252.3	278.9	531.3	42.5
IP	$\sqrt{3}/3$	167.9	185.6	97	107.2	237.5	262.5	500	40
IP	$\sqrt{3}/3$	157.4	174	90.9	100.5	222.7	246.1	468.8	37.5
IP	$\sqrt{3}/3$	146.9	162.4	84.8	93.8	207.8	229.7	437.5	35
90° OP	$\sqrt{3}/3$	209.9	232	121.2	134	296.9	328.1	625.0	50
90° OP	$\sqrt{3}/3$	199.4	220.4	115.1	127.3	282	311.7	593.8	47.5
90° OP	$\sqrt{3}/3$	188.9	208.8	109.1	120.6	267.2	295.3	562.5	45
90° OP	$\sqrt{3}/3$	178.4	197.2	103	113.9	252.3	278.9	531.3	42.5
90° OP	$\sqrt{3}/3$	167.9	185.6	97	107.2	237.5	262.5	500	40
90° OP	$\sqrt{3}/3$	157.4	174	90.9	100.5	222.7	246.1	468.8	37.5
90° OP	$\sqrt{3}/3$	146.9	162.4	84.8	93.8	207.8	229.7	437.5	35
Additive manufactured, As built									
IP	$\sqrt{3}/3$	199.4	220.4	115.1	127.3	282	311.7	593.8	47.5
IP	$\sqrt{3}/3$	188.9	208.8	109	120.6	267.2	295.3	562.5	45
IP	$\sqrt{3}/3$	146.9	162.4	84.8	93.8	207.8	229.7	437.5	35
IP	$\sqrt{3}/3$	126	139.2	72.7	80.4	178.1	196.9	375	30
IP	$\sqrt{3}/3$	105	116	60.6	67	148.4	164	312.5	25
IP	$\sqrt{3}/3$	94.5	104.4	54.5	64.3	133.6	147.7	281.3	22.5
IP	$\sqrt{3}/3$	84	92.8	48.5	53.6	118.8	131.3	250	20
IP	$\sqrt{3}/3$	63	69.6	36.4	40.2	89.1	98.4	187.5	15
IP	$\sqrt{3}/3$	52.5	58	30.3	33.5	74.2	82	156.3	12.5
90° OP	$\sqrt{3}/3$	167.9	185.6	97	107.2	237.5	262.5	500	40
90° OP	$\sqrt{3}/3$	146.9	162.4	84.8	93.8	207.8	229.7	437.5	35
90° OP	$\sqrt{3}/3$	136.4	150.8	78.8	87.1	193	213.3	406.3	32.5
90° OP	$\sqrt{3}/3$	126	139.2	72.7	80.4	178.1	196.9	375	30
90° OP	$\sqrt{3}/3$	115.5	127.6	66.7	73.7	163.3	180.5	343.8	27.5
90° OP	$\sqrt{3}/3$	105	116	60.6	67	148.4	164	312.5	25
90° OP	$\sqrt{3}/3$	94.5	104.4	54.5	64.3	133.6	147.7	281.3	22.5
90° OP	$\sqrt{3}/3$	84	92.8	48.5	53.6	118.8	131.3	250	20
90° OP	$\sqrt{3}/3$	73.5	81.2	42.4	46.9	103.9	114.8	218.8	17.5

Fatemi-Socie criterion with respect to the MSWT criterion. This is because the Fatemi-Socie damage parameter is more appropriate for ductile materials.

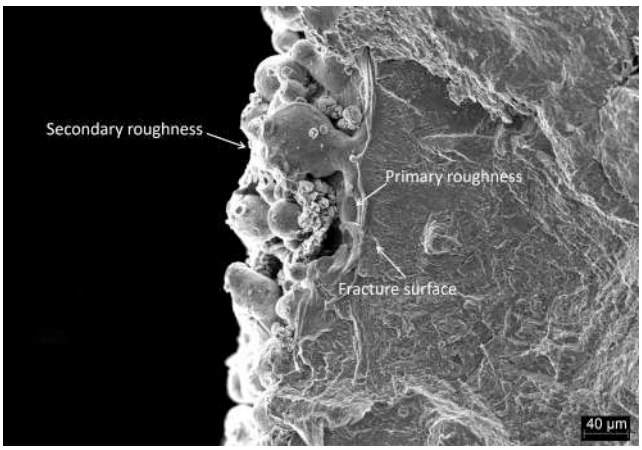

Fig. 5. Scanning microscope image of an as built surface sample.

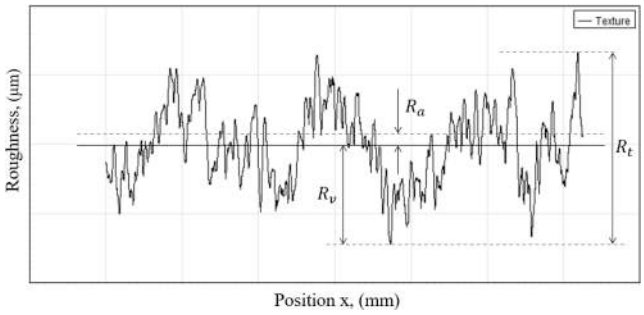

Fig. 6. Roughness profile of the sample.

Table 2
Mean values of the surface roughness parameter and standard deviation.

Surface condition	Roughness parameters	Mean value [μm]	Standard deviation
Machined 17 samples	$R_{a,o}$	0.31	0.04
	$R_{t,o}$	3.00	0.91
	$R_{v,o}$	1.69	0.72
	$R_{a,i}$	2.25	0.90
	$R_{t,i}$	16.90	7.13
	$R_{v,i}$	9.47	3.12
As built 18 samples	$R_{a,o}$	19.26	1.46
	$R_{t,o}$	138.94	13.73
	$R_{v,o}$	70.27	7.72
	$R_{a,i}$	21.21	2.26
	$R_{t,i}$	147.67	16.25
	$R_{v,i}$	69.54	9.21

2. Material and methods

2.1. Material and manufacturing process

Multiaxial fatigue tests were carried out using thin-walled tubular samples designed according to the ASTM Standard E2207-15 [22], see Fig. 1 for dimensions. Samples were made by Selective Laser Melting technology using an EOS machine and the experiments were carried out on both as built and post-machined batches. The manufacturing process was done using a laser source power of 340 W and a scan speed of 1900 mm/s. The layer thickness was 60 μm. The skywriting scanning strategy was adopted during the vertical growth of the samples, as schematically shown in Fig. 1, that allow in reducing the residual porosity at the boundaries [12]. A subsequent heat treatment at 650 °C for 3 h in vacuum condition, followed by slow rate cooling down to 350 °C, was also done to reduce residual stresses induced by the manufacturing process.

Table 3
Fatigue test results.

Load type	$\frac{\tau}{\sigma}$	ID sample	$\overline{\sigma}_a$ [MPa]	$\overline{\varepsilon}_a$(%)	$\frac{\overline{\sigma}_{max}}{S_u}$(%)	Reversals to failure ($2N_f$)
Additive manufactured, Machined						
IP	$\sqrt{3}/3$	P1	311.7	0.291	52.5	239,378
IP	$\sqrt{3}/3$	P2	296.9	0.287	50	154,888
IP	$\sqrt{3}/3$	P3	282	0.278	47.5	325,798
IP	$\sqrt{3}/3$	P4	267.2	0.259	45	198,130
IP	$\sqrt{3}/3$	P5	252.3	0.248	42.5	576,378
IP	$\sqrt{3}/3$	P6	237.5	0.232	40	291,936
IP	$\sqrt{3}/3$	P7	237.5	0.232	40	1,277,694
IP	$\sqrt{3}/3$	P8	222.7	0.217	37.5	3,546,246
IP	$\sqrt{3}/3$	P9	207.8	0.195	35	>4,000,000
90° OP	$\sqrt{3}/3$	P10	296.9	0.260	50	122,758
90° OP	$\sqrt{3}/3$	P11	282	0.253	47.5	214,726
90° OP	$\sqrt{3}/3$	P12	267.2	0.244	45	441,424
90° OP	$\sqrt{3}/3$	P13	267.2	0.237	45	238,434
90° OP	$\sqrt{3}/3$	P14	252.3	0.232	42.5	421,860
90° OP	$\sqrt{3}/3$	P15	237.5	0.218	40	676,576
90° OP	$\sqrt{3}/3$	P16	222.7	0.202	37.5	1,075,680
90° OP	$\sqrt{3}/3$	P17	207.8	0.183	35	>4,000,000
Additive manufactured, As built						
IP	$\sqrt{3}/3$	P1A	282	0.260	47.5	57,822
IP	$\sqrt{3}/3$	P2A	267.2	0.247	45	44,966
IP	$\sqrt{3}/3$	P3A	207.8	0.185	35	84,490
IP	$\sqrt{3}/3$	P4A	178.1	0.164	30	199,154
IP	$\sqrt{3}/3$	P5A	148.4	0.137	25	621,108
IP	$\sqrt{3}/3$	P6A	133.6	0.125	22.5	509,144
IP	$\sqrt{3}/3$	P7A	118.8	0.109	20	1,069,342
IP	$\sqrt{3}/3$	P8A	89	0.083	15	1,985,452
IP	$\sqrt{3}/3$	P9A	74.2	0.054	12.5	>4,000,000
90° OP	$\sqrt{3}/3$	P10A	237.5	0.226	40	70,514
90° OP	$\sqrt{3}/3$	P11A	207.8	0.181	35	98,102
90° OP	$\sqrt{3}/3$	P12A	193	0.161	32.5	214,074
90° OP	$\sqrt{3}/3$	P13A	178.1	0.144	30	296,170
90° OP	$\sqrt{3}/3$	P14A	163.3	0.140	27.5	260,150
90° OP	$\sqrt{3}/3$	P15A	148.4	0.127	25	392,346
90° OP	$\sqrt{3}/3$	P16A	133.6	0.120	22.5	614,212
90° OP	$\sqrt{3}/3$	P17A	118.8	0.097	20	913,110
90° OP	$\sqrt{3}/3$	P18A	103.9	0.094	17.5	>4,000,000

Monotonic quasi static tensile and torsional tests were carried out to estimate the main mechanical properties of the material. To this aim, an electro-mechanic MTS criterion s45 testing machine, equipped with a load cell of 100 kN and an MTS extensometer with 10 mm of gauge length, was used for the tensile characterization, whereas an electro-dynamic biaxial Instron ElectroPulse E10000 testing machine, equipped with a load cell of 100 Nm, was used for the torsional characterization. Fig. 2 shows the engineering stress–strain responses together with the main mechanical properties. Please consider that the offset method at 0.2% was used to measure the value of tensile and shear yield strength, namely S_y and S_{sy}, respectively.

The microstructure of AM Ti6Al4V alloy is influenced by process and the thermal histories. In particular, temperature has the main effect on microstructure evolution because it acts as a heat treatment on the α' martensite [23]. In the SLM processes, the high temperature transforms α' martensite in α + β lamellae structure as reported in Fig. 3. Micrograph images also reveals the presence of several defects (see Fig. 3a-b). Two types of defects can be distinguished: gas pores and lack-of-fusion (LOF). These latter differ from pores because they are characterized by an irregular shape and because they are typically aligned with the building direction (BD) as shown in Fig. 3a.

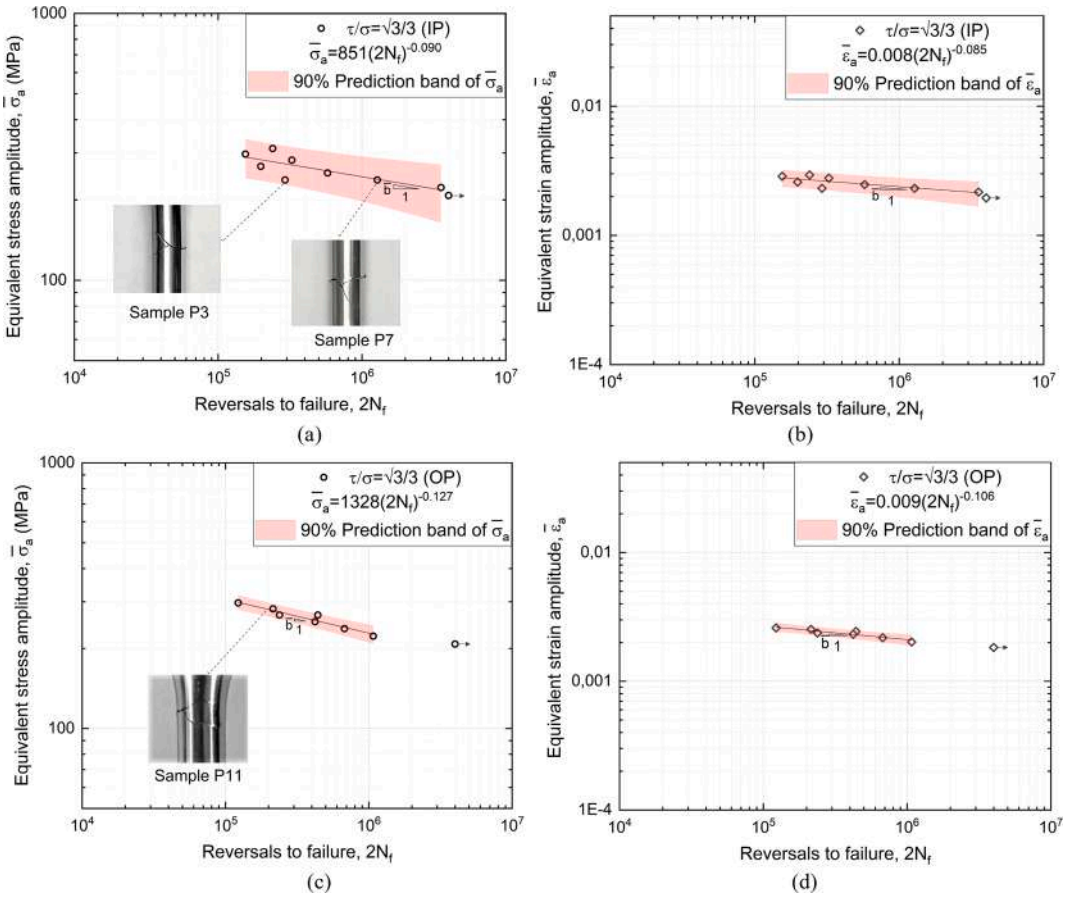

Fig. 7. Equivalent stress and strain amplitude as a function of the number of reversals to failure for machined samples: (a) (b) in-phase loading; (c) (d) 90° out-of-phase loading.

2.2. Fatigue tests: method and equipment

Multiaxial fatigue tests were carried out by a biaxial testing machine Instron ElectroPulse E10000 equipped with a tensile and torsional load cell of 10 kN and 100 Nm, respectively. All tests were carried out in load control and with a frequency of 10 Hz, using proportional (in-phase, IP) and nonproportional (90° out-of-phase, OP) axial and torsional loadings. These latter, in particular, were defined by using the normal and shear stress ratio $\tau/\sigma = \sqrt{3}/3$. All the experiments were carried out using sinusoidal waveforms, with a stress ratio $R = 0.05$ and a run-out at $2 \bullet 10^6$ cycles. It is important to point out that, for both loading conditions, the stress path lies within the von Mises yield surface, see Fig. 4.

The applied stress values, in terms of axial stress amplitude (σ_a), axial mean stress (σ_m), shear stress amplitude (τ_a) and shear mean stress (τ_m), are summarized in Table 1. This latter also reports the ratio between the maximum von Mises equivalent stress and the ultimate tensile stress ($\bar{\sigma}_{max}/S_u$).

Digital image correlation (DIC) technique was also used to measure the local strains within the gage length of the samples. To this aim, a speckle pattern with a random grey scale distribution was made by airbrushing one side of the sample. A Sony ICX 625-Prosilica GT 2450 camera with a frame rate of 15 fps and resolution of 2440 by 2050 pixels was used to capture the digital images. Please consider that, in order to collect a proper number of pictures, for the most accurate strain measurement, the load frequency of the experiment was periodically decreased at 0.25 Hz. The correlation analysis was carried out using the commercial software VIC-2D Correlated Solution, setting a subset size of 51 pixels and subset distance of 4 pixels.

3. Multiaxial fatigue criteria and modeling

In order to predict the fatigue life of AM components and the failure plane orientation, the modified Smith Watson and Topper criterion, proposed by Jiang and Sehitoglu [24–27], was used. This latter is based on the definition of a damage parameter, D_{MSWT}, by the following equation:

$$D_{MSWT} = 2a\Delta\varepsilon\langle\sigma_{max}\rangle + \frac{1-a}{2}\Delta\gamma\Delta\tau \tag{1}$$

where $\Delta\varepsilon$ and σ_{max} are the normal strain range and maximum normal stress, respectively, $\Delta\gamma$ and $\Delta\tau$ are the shear strain and stress range, respectively, acting on critical plane. McCauley brackets for$\langle\sigma_{max}\rangle = 0.5$ $(\sigma_{max} + |\sigma_{max}|)$are used to avoid the negative value of damage. The coefficient a is a material-dependent constant that can range from 0 to 1 according to the cracking behavior of the material. In particular, when $0 \le a \le 0.37$ the MSWT criterion is used for materials with shear failure mechanisms, whereas for $a \ge 0.5$ the influence of the second term diminishes, and Eq. (1) became most adequate for brittle materials characterized by tensile crack behavior. Mixed crack behavior can be predicted using $0.37 \le a \le 0.5$. Based on this criterion, the critical plane is the one that maximize the damage parameter D_{MSWT} and, once identified, the fatigue life can be estimated according to Ma and Market [28] that use the uniaxial Manson Coffin equation to define the relationship between the damage parameter and the fatigue life (Eq. (2)).

$$D_{MSWT} = 4a\frac{(\sigma_f')^2}{E}(2N_f)^{2b} + 4a\sigma_f'\varepsilon_f'(2N_f)^{b+c} \tag{2}$$

It is important to point out that, such approach can be successfully

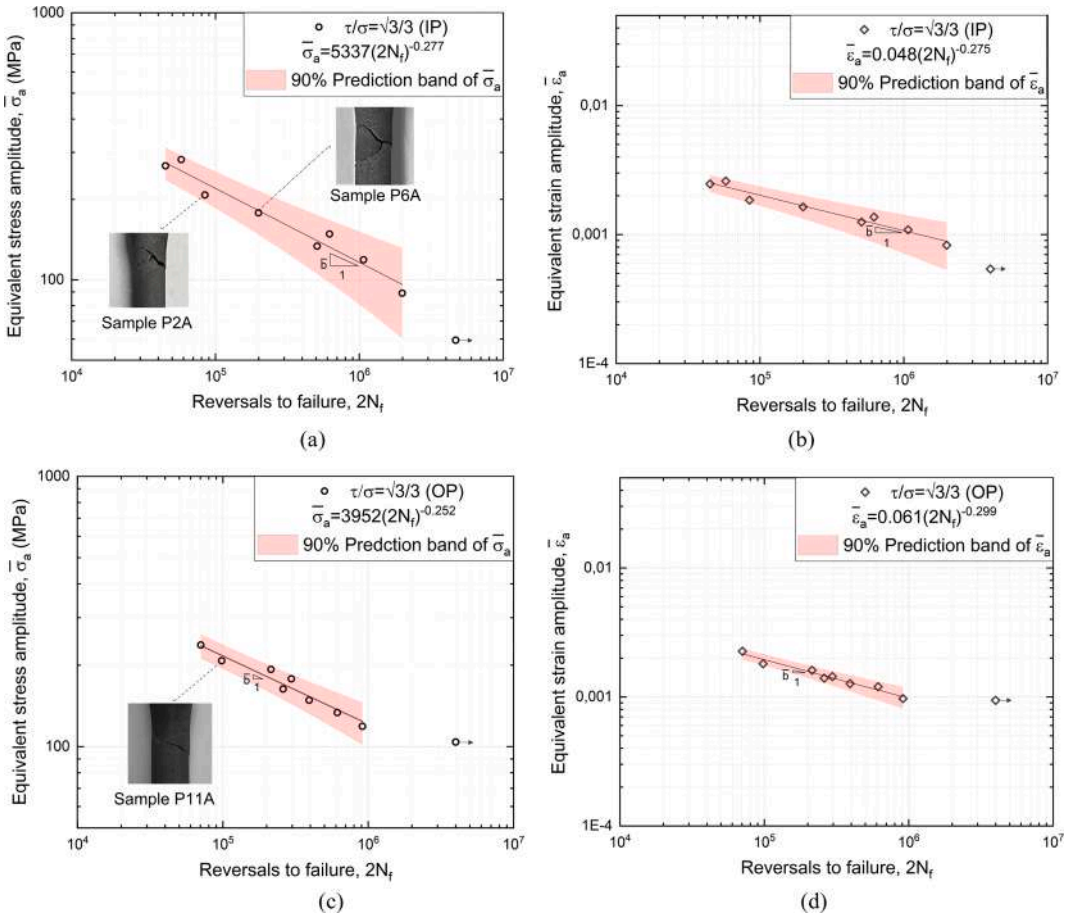

Fig. 8. Equivalent stress and strain amplitude as a function of the number of reversals to failure for as built samples: (a) (b) in-phase loading; (c) (d) 90° out-of-phase loading.

Table 4
Cyclic fatigue properties of the AM machined and as-built samples.

Machined samples					
Cyclic fatigue properties		*In-phase*		*90° Out-of-phase*	
		(R = 0.05)	*(R = -1)*	*(R = 0.05)*	*(R = -1)*
Effective fatigue strength coefficient [MPa]	$\bar{\sigma}_f'$	851	1612	1328	2561
Effective fatigue strength exponent	$\bar{b}$	−0.090	−0.113	−0.127	−0.157
Effective fatigue strength [MPa]	$\bar{S}_f$	207.8	254.6	207.8	254.6
As built samples					
Cyclic fatigue properties		*In-phase*		*90° Out-of-phase*	
		(R = 0.05)	*(R = -1)*	*(R = 0.05)*	*(R = -1)*
Effective fatigue strength coefficient [MPa]	$\bar{\sigma}_f'$	5337	12,981	3952	9539
Effective fatigue strength exponent	$\bar{b}$	−0.277	−0.328	−0.252	−0.310
Effective fatigue strength [MPa]	$\bar{S}_f$	74.2	79.4	103.9	114.4

Table 5
Comparison between the cyclic fatigue properties obtained under in-phase loading and the literature ones.

Cyclic fatigue properties (R = -1)		*In-phase axial and torsional*				
		AM Machined present results	AM As built present results	AM Machined [34]	AM As built [34]	Wrought [34]
Effective fatigue strength coefficient [MPa]	$\bar{\sigma}_f'$	1612	12,981	5912	3264	887.3
Effective fatigue strength exponent	$\bar{b}$	−0.118	−0.328	−0.244	−0.224	−0.021
Effective fatigue strength [MPa]	$\bar{S}_f$	254.6	79.4	230	154	365

used when sample made with traditional technique and mirror like surface quality are investigated. It is well known, in fact, that the as built AM samples are characterized by high roughness that typically represents one of the crucial aspects for crack initiation and propagation, as reported in several studies [16-19,29,30]. Some methods, based on the stress intensity factor (SIF), were developed to consider the effect of the surface roughness of the additive manufactured parts [16,19,30]. N. Sanaei and A. Fatemi [16] defined a new parameter $\sigma_a\sqrt{R_a}$ to be used for the correlation of uniaxial fatigue data and results revealed a good fitting independently of the surface quality. Under multiaxial loadings failures may occur under mixed mode crack growth. In this filed, an effective strain intensity factor range was proposed and successfully

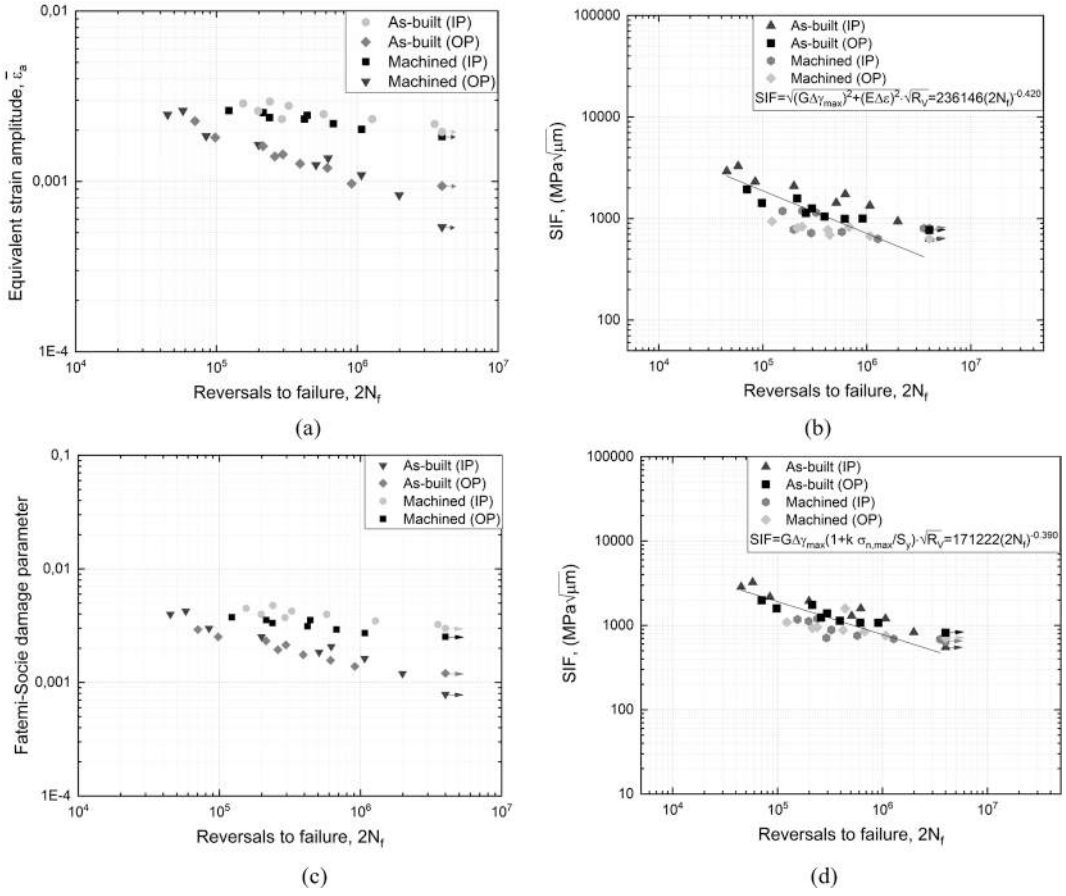

Fig. 9. Correlation parameters as a function of the number of reversals to failure: (a) Equivalent strain amplitude (Eq. (10)); (b) modified Socie's effective SIF range (Eq. (7)); (c) Fatemi-Socie damage parameter (Eq. (4)); (d) modified Reddy & Fatemi effective SIF range (Eq. (8)).

used by Socie et al. [31] for mixed-mode small cracks growth.

$$\Delta K_{eq}(\varepsilon)=\sqrt{\left(F_{II}\frac{E}{2(1+\nu)}\Delta\gamma_{max}\right)^2+(F_I E\Delta\varepsilon)^2}\sqrt{\pi a_0} \tag{3}$$

where $\Delta\gamma_{max}$ is the maximum shear strain range, $\Delta\varepsilon$ is the normal strain range acting on the plane of maximum shear strain plane, F_I and F_{II} are the geometry factor for mode I and mode II, respectively, and a_0 is the half initial surface crack length. Socie suggests that strain energy release rate is the driving force and the crack propagates in the direction of the maximum energy release rate. The release direction coincides with the direction in which the shear stress vanishes [31].

An additional effective SIF model was proposed by Reddy and Fatemi [32] which is based on critical plane approach. This latter is able predicts the failure plane orientation and fatigue life under proportional and nonproportional loading by defining the following damage parameter [33,34]:

$$D_{FS}=\frac{\Delta\gamma_{max}}{2}\left(1+k\frac{\sigma_{n,max}}{S_y}\right) \tag{4}$$

Starting from Eq. (4) the following effective strain intensity factor range was defined as follows [32]:

$$\Delta K_{CPA}=FG\Delta\gamma_{max}\left(1+k\frac{\sigma_{n,max}}{S_y}\right)\sqrt{\pi a_0} \tag{5}$$

It is important to point out that latter approaches are valid for materials where crack initiation and propagation occurs on the maximum shear strain planes. Based on the previous considerations, a new effective strain intensity factor range, based on the MSWT criterion, that is able to take into account the brittle failure behavior of the investigated material, is proposed in this work as follow:

$$\Delta K_{MSWT}=\left(F_I 2a\Delta\varepsilon\langle\sigma_{max}\rangle+F_{II}\frac{1-a}{2}\Delta\gamma\Delta\tau\right)\sqrt{\pi a_0} \tag{6}$$

The principal advantage of the proposed SIF model (Eq. (6)) is that it can be adapted to several cracking modes, depending on the type of material, and consider the synergic effect of normal and shear stress on the critical plane. In addition, Eq. (3), Eq. (5) and Eq. (6) were also modified in this study to take into account the effect of surface roughness by replacing the initial half crack length a_0 with $(R_v + a_0)$. The parameter R_v represents the maximum valley of the roughness profile that, as reported in [16,19] can be considered as a natural micro-notch, where the local stress concentration promotes the crack initiation and propagation.

If the initial conditions are taken into account, i.e., a_0=0 and $F = F_I = F_{II} = 1$, the correlation parameters, as a function of the surface roughness, can be obtained from Eq. (3), Eq. (5) and Eq. (6) as follow:

$$\Delta K_{eq}(\varepsilon)\big|_{a_0=0}=\sqrt{\left(\frac{E}{2(1+\nu)}\Delta\gamma_{max}\right)^2+(E\Delta\varepsilon)^2}\sqrt{R_v} \tag{7}$$

$$\Delta K_{CPA}\big|_{a_0=0}=G\Delta\gamma_{max}\left(1+k\frac{\sigma_{n,max}}{S_y}\right)\sqrt{R_v} \tag{8}$$

$$\Delta K_{MSWT}\big|_{a_0=0}=\left(2a\Delta\varepsilon\langle\sigma_{max}\rangle+\frac{1-a}{2}\Delta\gamma\Delta\tau\right)\sqrt{R_v} \tag{9}$$

In order to prove the reliability of the proposed approach (i.e., Eq. (9)) fatigue data were also correlated by the model reported in Eq. (8) and Eq. (7) for both the as built and machined samples.

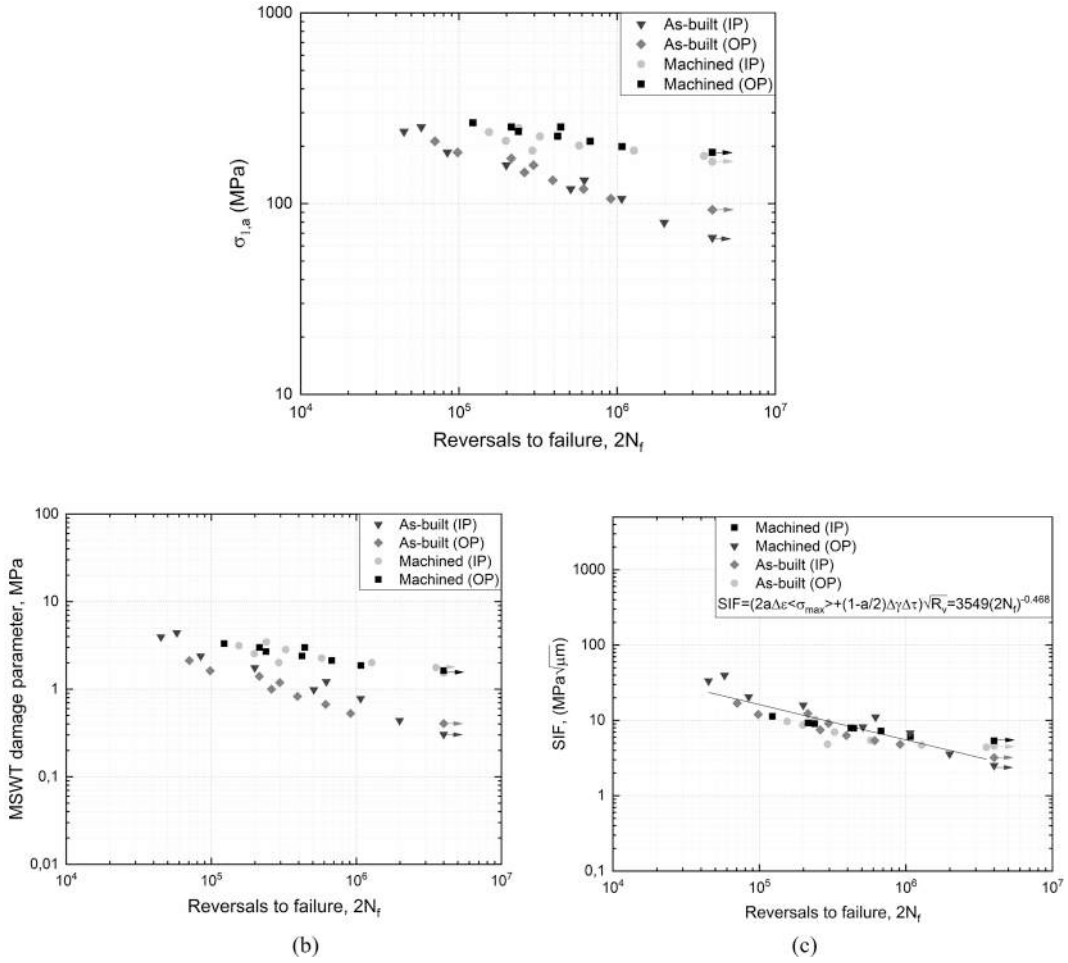

Fig. 10. (a) Maximum principal stress amplitude as a function of reversals to failure; (b) MSWT damage parameter (Eq. (1)) as a function of the number of reversals to failure; (c) Proposed MSWT effective strain intensity factor range (Eq. (9)) as a function of the number of reversals to failure.

4. Results and discussion

4.1. Surface morphology of samples

Fig. 5 shows a scanning microscope image of a sample in the as built conditions. Figure shows an irregular morphology of the free surface due to the presence of partially un-melted particles that remain attached to the surface, without carrying any load and representing stress concentration sites [19].

The surface roughness of the samples was measured by a rugosimeter TAYLOR HOBSON Sutronic 25 that provides a 2D linear profile of the surface. Measurements were carried out using a tip with 5 μm radius that, in a range of 300 μm, guarantee a resolution of 0.01 μm. Fig. 6 shows a representative roughness profile measured at the outer surface of the sample along its longitudinal direction (i.e., z-direction in Fig. 1). Measurements were carried out on both the outer and inner free surface, for a length of 12.5 mm with 8 repetitions at different locations. It is important to point out that, when dealing with in-phase axial and torsional loadings, the crack can initiate at the outer and/or inner surfaces of the samples [19], especially when small stress gradients, due to the small thickness of the samples, are involved. Therefore, in this case, also the inner roughness can have a high influence on fatigue performance and, for such reason, it was investigated in the measurement process [19].

Table 2 reports the mean and the standard deviation of the measured roughness for a population of seventeen machined samples and eighteen as built ones, respectively. Please consider that, subscript "*o*" refers to the outer surface, whereas subscript "*i*" refers to the inner one.

Obtained data revealed that, for both type of sample, the inner average roughness results higher than the outer one. In the case of the post treated samples, the reason can be partially attributed to the higher difficulty in machining the inner hole, compared to the outer surface.

4.2. Multiaxial fatigue results

Proportional and nonproportional multiaxial fatigue results, in terms of both von Mises stress and equivalent strain amplitude, are reported in Table 3, for both the machined and as built samples. The corresponding curves, as a function of the reversals to failure, are shown in Figs. 7–8. Figures also report the 90% prediction band and the Basquin's law parameters.

For the applied loading condition and the geometry of the sample, the equivalent strain amplitude was calculated using the following equation [35,36]:

$$\bar{\varepsilon}_a = \frac{1}{(1+\bar{\nu})\sqrt{2}}\sqrt{2(1+\bar{\nu})^2\varepsilon_{z,a}{}^2 + \frac{3}{2}\left(\gamma_{z\vartheta,a}\right)^2} \tag{10}$$

where $\bar{\nu}$ is the measured effective Poisson's ratio, $\varepsilon_{z,a}$ and $\gamma_{z\vartheta,a}$ are the normal and shear strain amplitude components, respectively. Please consider that, for plane stress condition $\gamma_{r\vartheta} = \gamma_{rz} = 0$. The effective Poisson's ratio $\bar{\nu}$ was calculated using the expression proposed by Ellyin et al. (Eq. (12)) [37]:

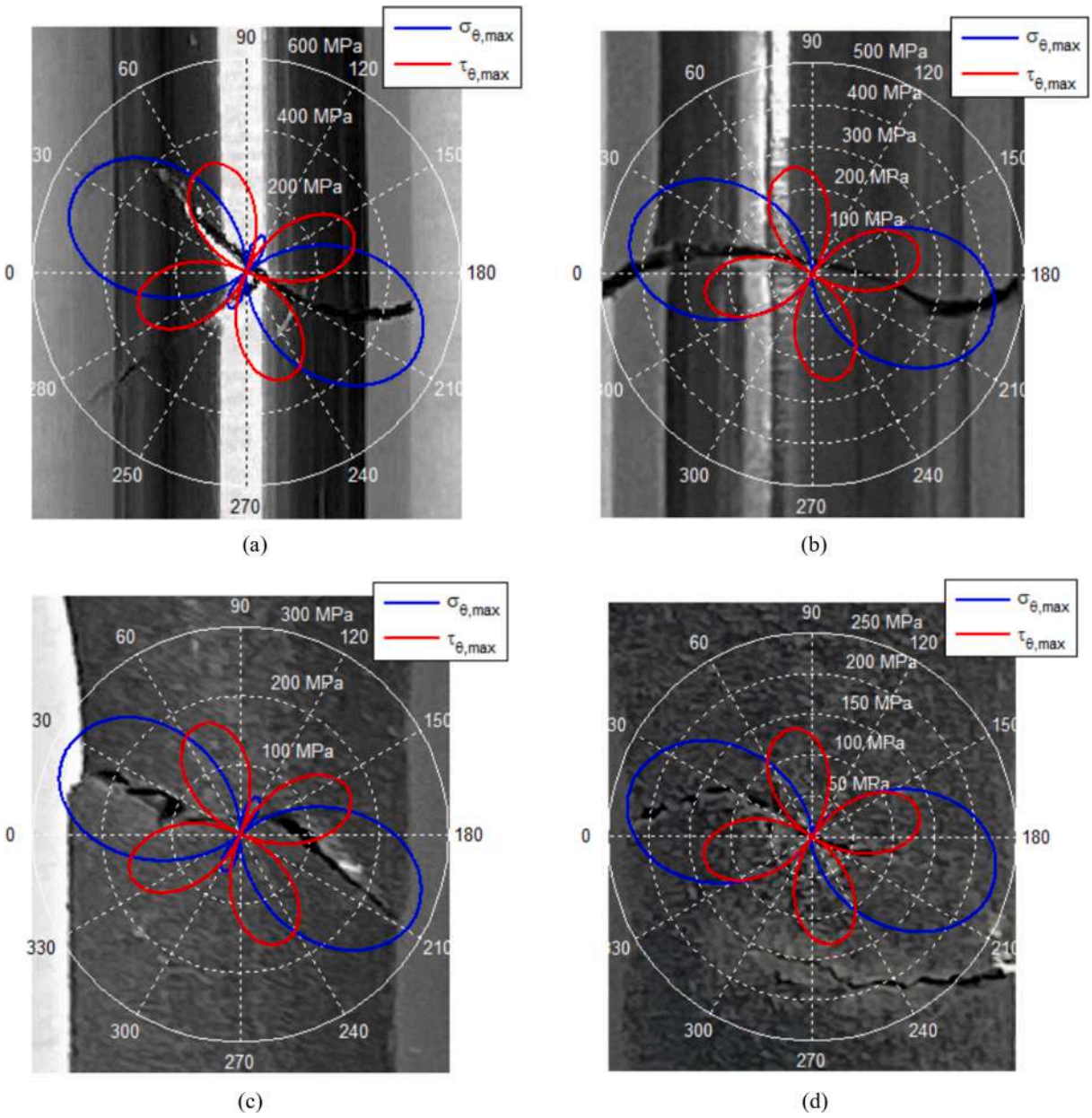

Fig. 11. Polar diagrams of the maximum normal and shear stress superimposed to fracture plane orientation of samples for (a) (c) in-phase and (b) (d) 90° out-of-phase loading.

Table 6
Maximum normal stress and shear stress acting on maximum normal stress plane.

Load type	*Sample type*	$\frac{\bar{\sigma}_{max}}{S_u}$(%)	θ_p[°]	$\sigma_{\theta,max}$[MPa]	$\tau_{\theta,max}$[MPa]
In-phase	Machined	47.5	24.6	530.5	0.083
	As built	25		279.2	0.043
90° out-of-phase	Machined	47.5	13.6	437.8	0.075
	As built	25		230.4	0.039

$$\bar{\nu} = \frac{\nu_p(1-\nu_e)(\Delta\varepsilon+\Delta\gamma) + (\nu_e-\nu_p)(\Delta\varepsilon_e+\Delta\gamma_e)}{(1-\nu_e)(\Delta\varepsilon+\Delta\gamma) + (\nu_e-\nu_p)(\Delta\varepsilon_e+\Delta\gamma_e)} \tag{11}$$

where ν_e and ν_p are elastic and plastic Poisson's ratio ($\nu_p = 0.5$), respectively, $\Delta\varepsilon$ and $\Delta\gamma$ are the applied normal and shear strain ranges, evaluated by DIC as reported in [35], $\Delta\varepsilon_e$ and $\Delta\gamma_e$ are the elastic normal and shear strain range that can be calculated using Hooke's law. The calculated value of effective Poisson's ratio is $\bar{\nu} = \nu_e = 0.32$, confirming that the material works within the elastic regime. For combined axial–torsional loading the circumferential and radial normal strain results equal to $\varepsilon_\vartheta = \varepsilon_r = -\nu_e\varepsilon_z$.

Experimental results show that machined samples experienced higher strength compared to the as built ones, revealing that the surface roughness has a primary role in the multiaxial fatigue performance of AM components. This behaviour can be justified as in the as built samples the presence of near-surface defects and the microstructural properties of the material, that typically are the most responsible of the fatigue strength of a material, have a secondary effect compared to the surface roughness, as also shown in [16]. The dominance effect of this latter is more considerable for samples with small internal cracks and coarser lamellar microstructure, and it became significant at the high cycle regime [16]. In addition, the scatter stress-life data of machined samples (Fig. 7) can be attributed to the minor effect of the surface

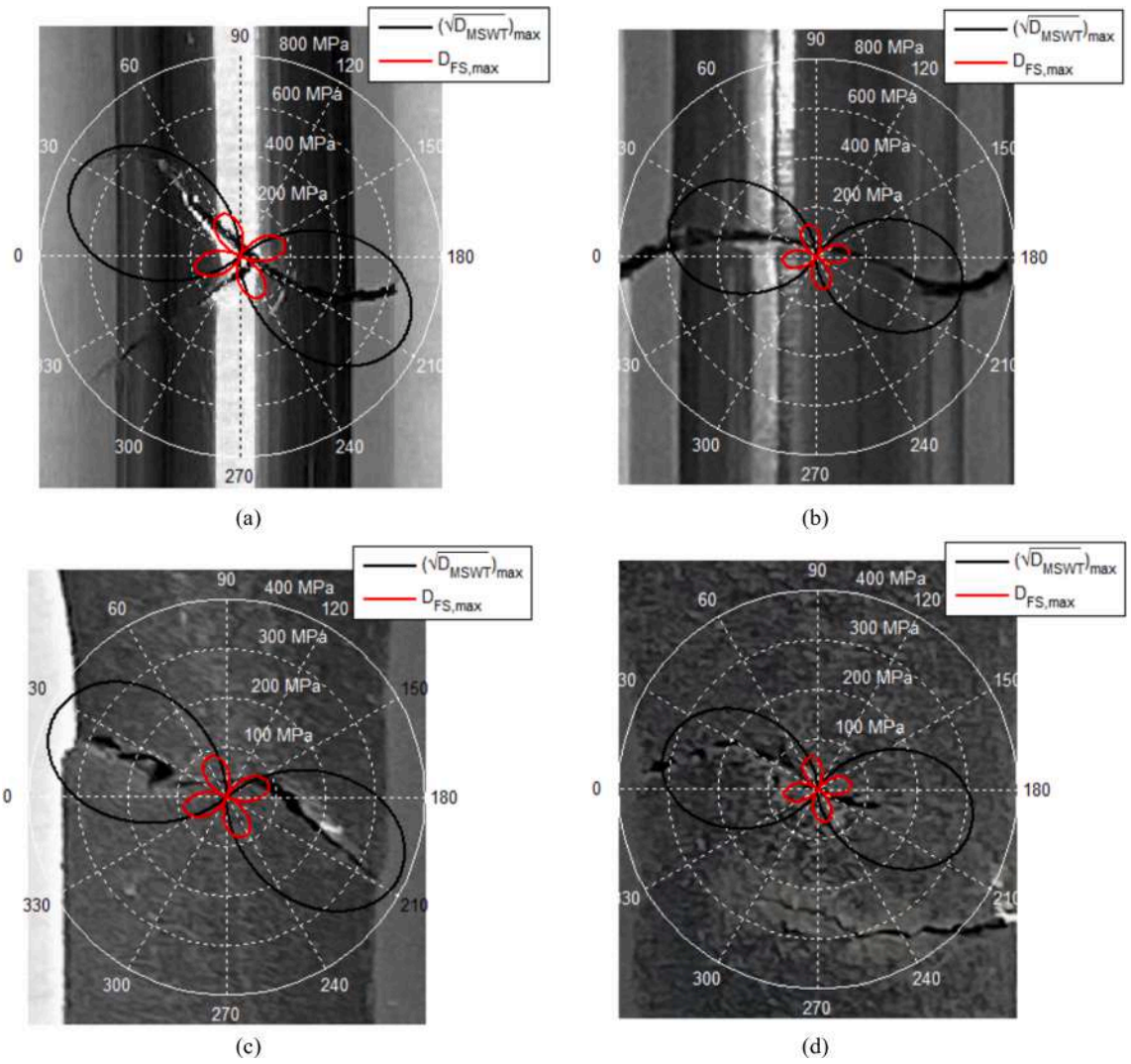

Fig. 12. Polar diagrams of the D_{FS} and $\sqrt{D_{MSWT}}$ parameter superimposed to fracture plane orientation of samples for (a) (c) in-phase and (b) (d) 90° out-of-phase loading.

roughness compared to the as built ones (Fig. 8).

If data are compared in terms of the applied loading conditions, one can observe no marked differences in terms of the fatigue life between the IP and OP cases. This result can be justified as the nonproportional loading strongly affects the material resistance at the low cycle regime whereas its influence is negligible at the high cycle regime, i.e. when the material works within the elastic condition. At the low cycle regime, in fact, shorter fatigue life under OP loading was observed as a consequence of the additional cyclic hardening induced by the slip system interaction activated by the rotation of the maximum shear strain planes. However, for materials that do not exhibit this latter effect, the shorter fatigue life is due to a wider range of material planes experience big damage values under OP loading [38]. Table 4 reports the experimental cyclic fatigue properties, in terms of effective fatigue strength coefficient $\overline{\sigma}_f'$, effective fatigue strength exponent $\overline{b}$ and the effective fatigue strength $\overline{S}_f$. In addition, with the aim to directly compare literature results obtained with a stress ratio $R = -1$, the fatigue strength properties, measured at $R = 0.05$, were recalculated at $R = -1$ using the modified Goodman criterion.

Table 5 report a direct comparison between the fatigue strength in-phase results for $R = -1$ and the literature ones [33]. These latter were also reported for both the AM (machined and as built) and wrought Ti6Al4V alloy.

The difference in the fatigue strength of present results compared to Fatemi et al. [34] is due to the different roughness conditions of the samples.

Fig. 9 show the correlation of the fatigue data for machined and as built samples, using the equivalent strain amplitude (Eq. (10)), the Fatemi-Socie damage parameter (Eq. (4)) and the modified SIF of Socie (Eq. (7)) and Reddy & Fatemi (Eq. (8)). It can be observed that results are well correlated using Eq. (7) (Fig. 9b) and Eq. (8) (Fig. 9d), which take into account the effect of surface roughness R_v for both types of samples, whereas no good match was observed using the equivalent strain amplitude, Fig. 9a, and Fatemi-Socie damage parameter, Fig. 9c.

Equivalent shear strain/stress is generally appropriate for the correlation of proportional fatigue data of ductile materials as a TC4 or wrought Ti6Al4V alloy [27,34]. Additively manufactured Ti6Al4V alloy, instead results brittle, as also shown by the tensile cracking modalities of samples and discussed in the next section, and the maximum principal stress or MSWT criterion [27] are most accurate in correlating the multiaxial fatigue data of AM Ti6Al4V alloy. In Fig. 10a and Fig. 10b the obtained results are reported according to the maximum principal stress and the MSWT criterion, respectively. One can observe that these latter provide a good correlation when dealing with the same surface condition, whereas the proposed MSWT damage parameter, that includes the effect of surface roughness has to be used for a better correlation of all

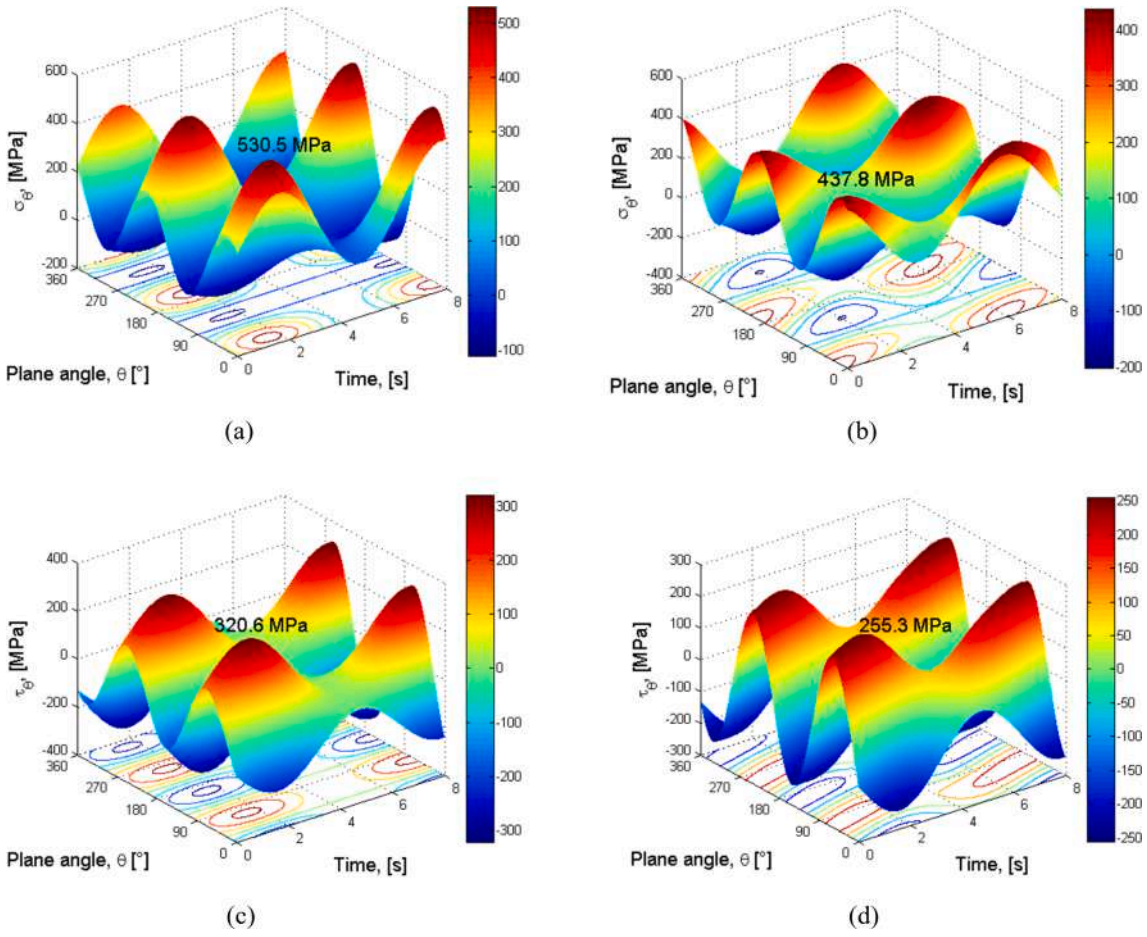

Fig. 13. Variation of the normal ad shear stress during (a) (c) in-phase and (b) (d) 90°out-of-phase cyclic loading ($\bar{\sigma}_{max} = 47.5\%S_u$).

fatigue data, as shown in Fig. 10c. Please consider that, in this latter case, in Eq. (9) the parameter a was setted equal to 1 as it describes the tensile cracking behavior of the material.

4.3. Analysis of failure plane orientation

When dealing with the fatigue life of materials it is possible to distinguish two different stages: crack initiation and crack propagation. The first stage can be divided into micro-crack nucleation (defects size ≈ 10 μm–100 μm) and small crack growth (defects size ≈ 100 μm–1 mm). In the ductile behaving materials the cracks nucleation occurs along maximum shear stress planes, whereas in the brittle behaving materials cracks nucleate along the maximum normal stress planes. Typically, experimental observations show that the crack path is not random but follows preferred planes depending on the material, loading, temperature, etc. [39]. In this work the failure modes of both types of the sample were analysed. Stress transformation equations were used to calculate the maximum normal/shear stress lying on any plane, for the different loading conditions. The stresses are evaluated using an increment of $\theta = 0.001°$ from 0° to 360° and the maximum value of normal and shear stress are plotted in the polar coordinate graph as shown in Fig. 11. Under in-phase loading the fracture occurs along the slip systems aligned with the maximum normal stress plane θ_p, oriented with an angle near the analytical value of 24.6° with respect to the plane normal to the loading axis (Fig. 11a-c).

For the machined sample ($\bar{\sigma}_{max} = 47.5\%S_u$) a higher variability of fracture path direction was observed with respect to the as built ($\bar{\sigma}_{max} = 25\%S_u$) sample. This can be attributed to a wide range of planes experienced stress values close to the maximum one, as shown in Fig. 13. The failure orientation for 90° out-of-phase loading is also aligned along with the slip system, where the maximum normal stress acts, with an angle of 13.6° (Fig. 11b-d). The calculated maximum normal stress and the shear stress, acting on the maximum normal stress plane θ_p for in-phase and 90°out-of-phase loading, are reported in Table 6.

The MSWT (Eq. (12)) and the Fatemi-Socie criterion based on only stress terms [38] (Eq. (13)) were also used to analyse the failure plane orientation as follows:

$$\sqrt{D_{MSWT}} = \sqrt{2E\Delta\varepsilon\langle\sigma_{n,max}\rangle} = 2\sigma_f'(2N_f)^b \tag{12}$$

$$D_{FS} = G\frac{\Delta\gamma_{max}}{2}\left(1 + k\frac{\sigma_{n,max}}{S_y}\right) = \tau_f'(2N_f)^{b_0} \tag{13}$$

The D_{FS} paramater for in-phase and 90° out-of-phase loading are presented in the polar diagrams for both types of samples. Results, reported in Fig. 12, show a minor prediction capability of the failure plane orientation compared to the $\sqrt{D_{MSWT}}$ parameter. This is because the Fatemi-Socie criterion is designed for materials that exhibit shear failure mechanisms. Therefore, the MSWT model is more adequate in the failure plane prediction of the AM Ti6Al4V alloy setting a material constant $a = 1$. Fig. 14 shows the variations of the D_{FS} and $\sqrt{D_{MSWT}}$ parameters during the proportional and nonproportional cyclic loading for the investigated material.

From Fig. 14 it is possible to identify that a wide range of planes are subject to a higher damage under 90° out-of-phase loading, but the maximum damage value is lower compared to the in-phase loading for the same level of stress, as also reported in Table 7.

Post-mortem surfaces were also investigated by SEM to analyze the crack initiation under combined loading. Fig. 15a shows a micro-crack

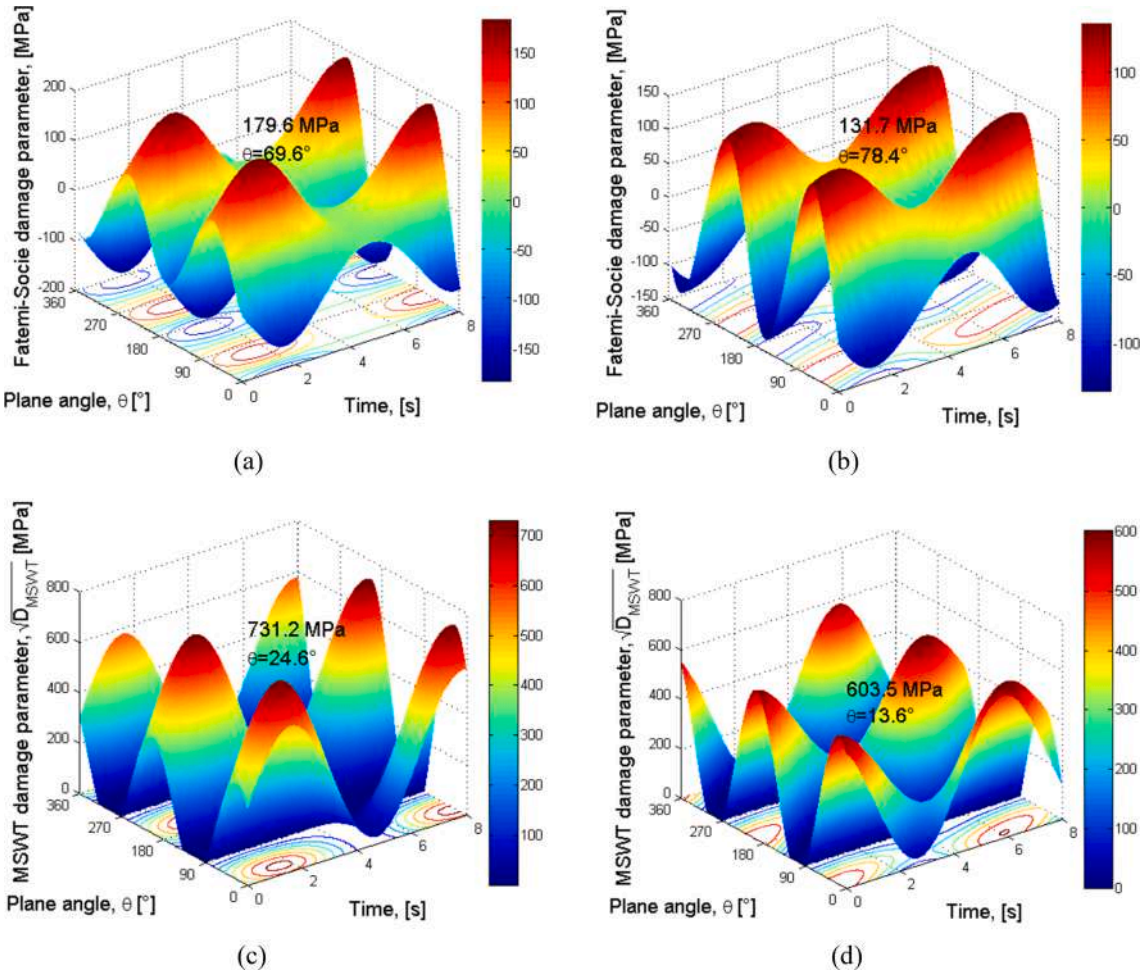

Fig. 14. Variation of D_{FS} and $\sqrt{D_{MSWT}}$ parameters during (a) (c) in-phase and (b) (d) 90°out-of-phase cyclic loading ($\overline{\sigma}_{max} = 47.5\%S_u$).

Table 7
Maximum damage value acting on the critical plane.

Critical plane Model	*Sample type*	*Load type*	$\frac{\overline{\sigma}_{max}}{S_u}$ (%)	*Critical plane orietation* θ_{CP} [°]	*Damage* [MPa]
D_{FS}	Machined	IP	47.5	69.6	179.6
	As built		25		87.72
	Machined	90° OP	47.5	78.4	131.7
	As built		25		66.73
$\sqrt{D_{MSWT}}$	Machined	IP	47.5	24.6	731.2
	As built		25		384.8
	Machined	90° OP	47.5	13.6	603.5
	As built		25		317.6

(size ≈ 25.8 μm) propagated on the surface of a machined sample under in-phase loading ($\overline{\sigma}_{max} = 47.5\%S_u$). The polar diagram of the maximum normal and shear strain superimposed to the micro-crack indicates that the propagation occurs on the maximum normal strain plane (see Fig. 16a).

Fig. 15b show a SEM image of a small-crack (size ≈ 100 μm) propagated on the surface of a machined sample under 90° out-of-phase loading ($\overline{\sigma}_{max} = 47.5\%S_u$). In this case, the small crack shows an unexpected behavior because the propagation seems to occur on the maximum shear strain plane (see Fig. 16b). Indeed, there is the possibility of anomalous growth behavior of the small crack, as also observed by S. Pearson [31,40]. However, in most cases, the propagation occurs along the maximum normal strain planes, as shown in Fig. 17.

4.4. Multiaxial fatigue life prediction

Fig. 17 report the predicted fatigue life according to the Fatemi-Socie (Eq. (13)), Fig. 18a, and the MSWT (Eq. (12)) criterion, Fig. 18b. Only fully reversed uniaxial fatigue tests were carried out to evaluate the cyclic fatigue properties in the elastic regime. The shear fatigue properties for the Fatemi-Socie criterion were evaluated using an empirical estimation method based on the von Mises criterion: $\tau_f' \approx \sigma_f'/\sqrt{3}$, $\gamma_f' \approx \sqrt{3}\varepsilon_f'$, $b_0 \approx b$ and $c_0 \approx c$ (see Fig. 18a-b) [33].

Based on the obtained results, we can observe that the MSWT criterion gives a more accurate life prediction for both the loading conditions compared to the Fatemi-Socie criterion. This result further proves that the Fatemi-Socie criterion is more adequate for materials with the shear crack mechanism as the wrought Ti6Al4V alloy. The principal advantage of the MWST criterion is that it can be adapted for different materials with different cracking modes, setting an adequate value of the coefficient *a*. In addition, both damage models overestimate the prediction of the fatigue life of the as built sample, because these models are designed for machined and polished samples.

5. Conclusion

In this work the effect of surface roughness on the multiaxial fatigue behavior of AM Ti6Al4V samples under in-phase and 90° out-of-phase loading was investigated. Fatigue tests were carried out combined

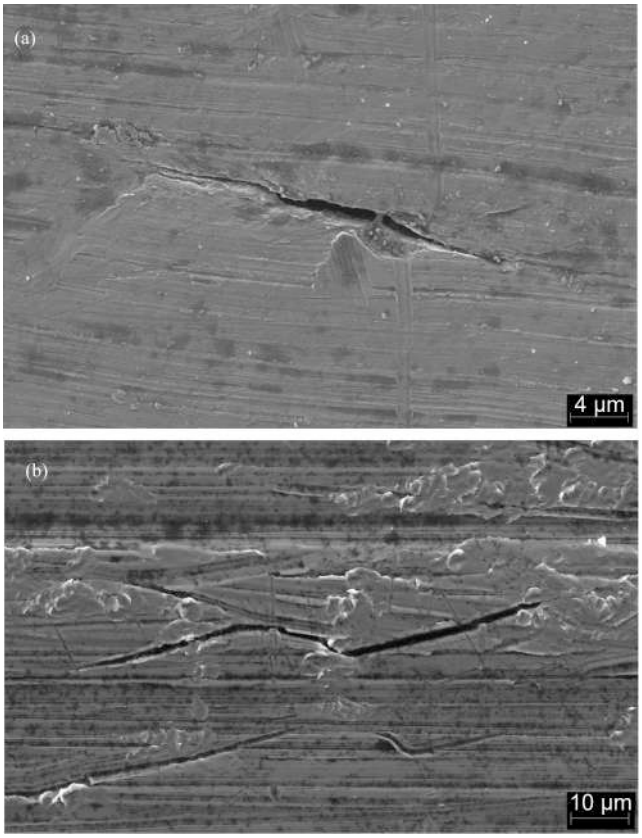

Fig. 15. SEM image of: (a) micro-crack (size ≈25.8 μm) propagated on the surface of a machined sample under in-phase loading; (b) small crack (size ≈100 μm) propagated on the surface of a machined sample under 90° out-of-phase loading ($\bar{\sigma}_{max} = 47.5\%S_u$).

axial–torsional loading and using two different batches of samples with different roughness conditions: machined and as built. The synergistic effect of surface roughness with the defects and the multiaxial state of stress results in a reduction of fatigue performance. Multiaxial fatigue strength increases with a decrease in surface roughness. No differences in terms of fatigue life under proportional and nonproportional loading were observed. This is because the nonproportional hardening has a major effect in the low cycle regime and the effect is negligible in the high cycle regime where the material work within the elastic condition. An effective strain intensity factor range based on the modified Smith Watson and Topper criterion, that incorporates the roughness parameter R_v is proposed and used to improve the correlation of the fatigue data. The Socie and the Reddy & Fatemi effective strain intensity factors range are also modified and used for the correlation of fatigue data, but a major scatter of the results was observed compared to the proposed MSWT effective strain intensity factor range. The surface of the samples was also investigated by SEM to analyze the crack orientation under combined loading. Results show that the crack growth occurs along the slip systems aligned with the maximum normal stress plane. A minor prediction capacity of the failure plane orientation and the fatigue life was obtained using the Fatemi-Socie criterion compared to the MSWT criterion. This is because the Fatemi-Socie damage parameter is more appropriate for shear failure mechanism materials whereas the AM Ti6Al4V alloy shows a normal cracking behavior. In conclusion, an additional advantage of the proposed effective strain intensity factor range is that can be also express as function of effective crack area based on Murakami's method [41] (i.e., replacing a_0 with $\sqrt{Area_{eff}}$) becoming more useful for the microtomography analysis of crack growth behavior, that will carry out in a future study.

Fig. 17. SEM image of micro-cracks propagation along several dislocation planes aligned with the maximum normal strain plane ($\bar{\sigma}_{max} = 47.5\%S_u$).

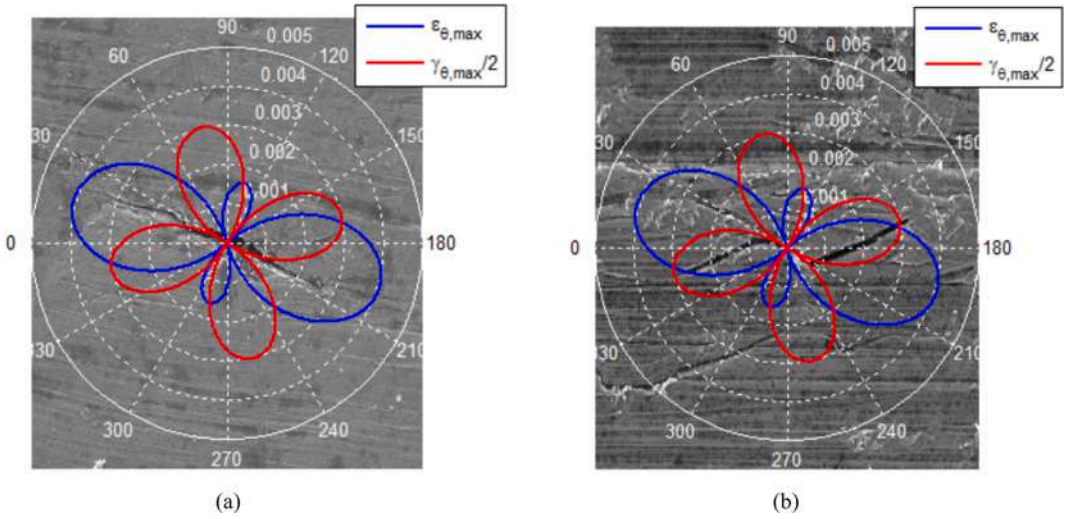

Fig. 16. Polar diagram of the maximum normal and shear strain superimposed to (a) micro-crack (size ≈25.8 μm) propagated under in-phase loading and (b) small crack (size ≈100 μm) propagated under 90° out-of-phase loading ($\bar{\sigma}_{max} = 47.5\%S_u$).

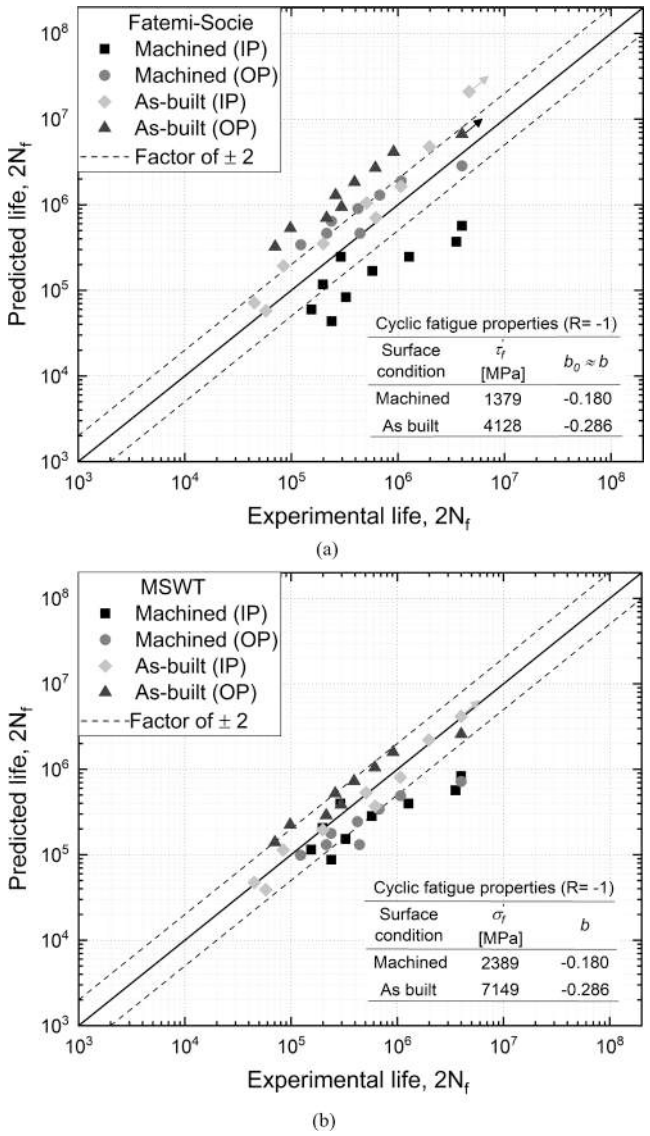

Fig. 18. Fatigue life prediction for AM Ti6Al4V alloy using the (a) Fatemi-Socie criterion and (b) MSWT criterion.

Declaration of Competing Interest

The authors declare that they have no known competing financial interests or personal relationships that could have appeared to influence the work reported in this paper.

Data availability statement.

The data that support the findings of this study are available from the corresponding author upon request.

Acknowledgements

This work was supported by the regional program "POR Calabria FSE/FESR 2014-2010", within the context of "Smart Specialization Strategy - S3 Calabria (Italy)", topic: "Smart Manufacturing".

References

[1] Donachie MJ. Titanium: a technical guide. second ed. Materials Park, OH: ASM International; 2000.
[2] Liu G, Zhang X, Chen X, He Y, Cheng L, Huo M, et al. Additive manufacturing of structural materials. Mater Sci Eng: R: Rep 2021;145:100596. https://doi.org/10.1016/j.mser.2020.100596.
[3] Wang Y, Zhang L, Daynes S, Zhang H, Feih S, Wang MY. Design of graded lattice structure with optimized mesostructures for additive manufacturing. Mater Des 2018;142:114–23. https://doi.org/10.1016/j.matdes.2018.01.011.
[4] Ni J, Ling H, Zhang S, Wang Z, Peng Z, Benyshek C, et al. Three-dimensional printing of metals for biomedical applications. Mater Today Bio 2019;3:100024. https://doi.org/10.1016/j.mtbio.2019.100024.
[5] Khajavi SH, Partanen J, Holmström J. Additive manufacturing in the spare parts supply chain. Comput Ind 2014;65(1):50–63. https://doi.org/10.1016/j.compind.2013.07.008.
[6] Ambrogio G, Sgambitterra E, De Napoli L, Gagliardi F, Fragomeni G, Piccininni A, et al. Performances analysis of titanium prostheses manufactured by superplastic forming and incremental forming. Procedia Eng 2017;183:168–73.
[7] Gibson I, Rosen D, Stucker B, Khorasani M. Hybrid additive manufacturing. In: Gibson I, Rosen D, Stucker B, Khorasani M, editors. Additive manufacturing technologies. Cham: Springer International Publishing; 2021. p. 347–66. https://doi.org/10.1007/978-3-030-56127-7_12.
[8] Lewandowski JJ, Seifi M. Metal additive manufacturing: a review of mechanical properties. Annu Rev Mater Res 2016;46(1):151–86. https://doi.org/10.1146/annurev-matsci-070115-032024.
[9] Froes FH, Dutta B. The additive manufacturing (AM) of titanium alloys. Adv Mater Res 2017;72(2):96–106. https://doi.org/10.1016/j.mprp.2016.12.062.
[10] Fatemi A, Molaei R, Phan N, Palin-Luc T, Morel F, Carpinteri A. Multiaxial fatigue of additive manufactured metals. MATEC Web Conf 2019;300:01003. https://doi.org/10.1051/matecconf/201930001003.
[11] Ramos D, Belblidia F, Sienz J. New scanning strategy to reduce warpage in additive manufacturing. Addit Manuf 2019;28:554–64. https://doi.org/10.1016/j.addma.2019.05.016.
[12] Mancisidor AM, Garciandia F, San Sebastian M, Álvarez P, Díaz J, Unanue I. Reduction of the residual porosity in parts manufactured by selective laser melting using skywriting and high focus offset strategies. Phys Procedia 2016;83:864–73. https://doi.org/10.1016/j.phpro.2016.08.090.
[13] Kumbhar NN, Mulay AV. Post processing methods used to improve surface finish of products which are manufactured by additive manufacturing technologies: a review. J Inst Eng (India): Ser C 2018;99(4):481–7. https://doi.org/10.1007/s40032-016-0340-z.
[14] Moylan S, Slotwinski J, Cooke A, Jurrens K, Donmez M. Proposal for a standardized test artifact for additive manufacturing machines and processes. Proceedings of the solid freeform fabrication symposium. 2012.
[15] Monzón MD, Ortega Z, Martínez A, Ortega F. Standardization in additive manufacturing: activities carried out by international organizations and projects. Int J Adv Manuf Technol 2015;76(5–8):1111–21. https://doi.org/10.1007/s00170-014-6334-1.
[16] Sanaei N, Fatemi A. Analysis of the surface roughness on fatigue performance of powder bed fusion additive manufactured metals. Theor Appl Fract Mech 2020;108. https://doi.org/10.1016/j.tafmec.2020.102638.
[17] Greitemeier D, Dalle Donne C, Syassen F, Eufinger J, Melz T. Effect of surface roughness on fatigue performance of additive manufactured Ti6Al4V. Mater Sci Technol 2016;32(7):629–34. https://doi.org/10.1179/1743284715Y.0000000053.
[18] Bagehorn S, Wehr J, Maier HJ. Application of mechanical surface finishing processes for roughness reduction and fatigue improvement of additively manufactured Ti-6Al-4V parts. Int J Fatigue 2017;102:135–42. https://doi.org/10.1016/j.ijfatigue.2017.05.008.
[19] Zhang J, Fatemi A. Surface roughness effect on multiaxial fatigue behavior of additive manufactured metals and its modeling. Theor Appl Fract Mech 2019;103:102260. https://doi.org/10.1016/j.tafmec.2019.102260.
[20] Pegues J, Roach M, Williamson RS, Shamsaei N. Surface roughness effects on the fatigue strength of additively manufactured Ti-6Al-4V. Int J Fatigue 2018;116:543–52. https://doi.org/10.1016/j.ijfatigue.2018.07.013.
[21] Greitemeier D, Palm F, Syassen F, Melz T. Fatigue performance of additive manufactured TiAl6V4 using electron and laser beam melting. Int J Fatigue 2017;94:211–7. https://doi.org/10.1016/j.ijfatigue.2016.05.001.
[22] ASTM E2207 - 15. Standard practice for strain-controlled axial-torsional testing with thin walled tube specimens. Annual Book of ASTM Standards. American Society of Testing and Materials 2006: 03(01): 1252–9.
[23] Liu S, Shin YC. Additive manufacturing of Ti6Al4V alloy: a review. Mater Des 2019;164:107552. https://doi.org/10.1016/j.matdes.2018.107552.
[24] Jiang Y, Sehitoglu H. A model for rolling contact failure. Wear 1999;224(1):38–49. https://doi.org/10.1016/S0043-1648(98)00311-1.
[25] Jiang YY. A fatigue criterion for general multiaxial loading. Fatigue Fract Eng Mater Struct (Print) 2000;23(1):19–32. https://doi.org/10.1046/j.1460-2695.2000.00247.x.
[26] Yu Q, Zhang J, Jiang Y, Li Q. Multiaxial fatigue of extruded AZ61A magnesium alloy. Int J Fatigue 2011;33(3):437–47. https://doi.org/10.1016/j.ijfatigue.2010.09.020.
[27] Zhu SP, Yu ZY, Correia J, De Jesus A, Berto F. Evaluation and comparison of critical plane criteria for multiaxial fatigue analysis of ductile and brittle materials. Int J Fatigue 2018;112:279–88. https://doi.org/10.1016/j.ijfatigue.2018.03.028.
[28] Ma S, Markert B, Yuan H. Multiaxial fatigue life assessment of sintered porous iron under proportional and non-proportional loadings. Int J Fatigue 2017;97:214–26. https://doi.org/10.1016/j.ijfatigue.2017.01.005.
[29] Molaei R, Fatemi A, Sanaei N, Pegues J, Shamsaei N, Shao S, et al. Fatigue of additive manufactured Ti-6Al-4V, Part II: The relationship between microstructure,

material cyclic properties, and component performance. Int J Fatigue 2020;132:105363. https://doi.org/10.1016/j.ijfatigue.2019.105363.
[30] Chan KS, Koike M, Mason RL, Okabe T. Fatigue life of titanium alloys fabricated by additive layer manufacturing techniques for dental implants. Metall Mater Trans A 2013;44(2):1010–22. https://doi.org/10.1007/s11661-012-1470-4.
[31] Socie DF, Hua CT, Worthem DW. Mixed mode small crack growth. Fatigue Fract Engng Mater Struct 1987;10(1):1–16. https://doi.org/10.1111/j.1460-2695.1987.tb01145.x.
[32] Qian J, Fatemi A. Mixed mode fatigue crack growth: a literature survey. Eng Fract Mech 1996;55(6):969–90. https://doi.org/10.1016/S0013-7944(96)00071-9.
[33] Stephens RI, Fatemi A, Stephens RR, Fuchs HO, Metal fatigue in engineering, second ed., AWiley-Interscience Publication.
[34] Fatemi A, Molaei R, Sharifimehr S, Phan N, Shamsaei N. Multiaxial fatigue behavior of wrought and additive manufactured Ti-6Al-4V including surface finish effect. Int J Fatigue 2017;100:347–66. https://doi.org/10.1016/j.ijfatigue.2017.03.044.
[35] Renzo DA, Sgambitterra E, Maletta C, Furgiuele F, Biffi CA, Fiocchi J, et al. Multiaxial fatigue behavior of SLM Ti6Al4V alloy under different loading conditions. Fatigue Fract Eng Mater Struct 2021;44(10):2625–42. https://doi.org/10.1111/ffe.13518.
[36] McDowell D, Ellis J, editors. STP1191-EB advances in multiaxial fatigue. West Conshohocken, PA: ASTM International; 1993. https://doi.org/10.1520/STP1191-EB.
[37] Ellyin F, Xia Z. A general fatigue theory and its application to out-of-phase cyclic loading. J Eng Mater Technol 1993;115:411–6. https://doi.org/10.1115/1.2904239.
[38] Mahtabi MJ, Shamsaei N. Multiaxial fatigue modeling for Nitinol shape memory alloys under in-phase loading. J Mech Behav Biomed Mater 2016;55:236–49. https://doi.org/10.1016/j.jmbbm.2015.10.022.
[39] Shamsaei N, Fatemi A. Deformation and fatigue behaviors of case-hardened steels in torsion: experiments and predictions. Int J Fatigue 2009;31(8–9):1386–96. https://doi.org/10.1016/j.ijfatigue.2009.03.020.
[40] Pearson S. Initiation of fatigue cracks in commercial aluminium alloys and the subsequent propagation of very short cracks. Eng Fract Mech 1975;7(2):235–47. https://doi.org/10.1016/0013-7944(75)90004-1.
[41] Murakami Yukitaka. Metal Fatigue: Effects of Small Defects and Nonmetallic Inclusions. Academic Press; 2019.